Post-process lasering improves strength-ductility tradeoff and fatigue limit of additively manufactured stainless steels

Juan Guillermo Santos Macías, Kewei Chen, Alexandre Tanguy, Maxime Vallet, Louis Cornet, Vincent Michel, Manas Vijay Upadhyay

Post-process lasering improves strength-ductility tradeoff and fatigue limit of additively manufactured stainless steels

Juan Guillermo Santos Macías[1,+], Kewei Chen[1], Alexandre Tanguy[1], Maxime Vallet[2,3], Louis Cornet[2], Vincent Michel[4], Manas Vijay Upadhyay[1,*]

[1] Laboratoire de Mécanique des Solides (LMS), CNRS, École Polytechnique, Institut Polytechnique de Paris, Route de Saclay, 91120 Palaiseau, France

[2] Université Paris-Saclay, CentraleSupélec, ENS Paris-Saclay, CNRS, LMPS - Laboratoire de Mécanique Paris-Saclay, 91190 Gif-sur-Yvette, France

[3] Université Paris-Saclay, CentraleSupélec, CNRS, Laboratoire SPMS - Structures, Propriétés et Modélisation des Solides, 91190 Gif-sur-Yvette, France

[4] Laboratoire de Procédés et Ingénierie en Mécanique et Matériaux (PIMM), CNRS UMR 8006, Arts et Metiers Institute of Technology, HESAM University, 151 Boulevard de l'Hôpital, 75013 Paris, France

[*] First corresponding author email: manas.upadhyay@polytechnique.edu,

[+] Second corresponding author email: guillermo.santos@imdea.org

Abstract

Although stainless steels fabricated via additive manufacturing exhibit higher strength in comparison to their conventionally manufactured counterparts, they often suffer from lower ductility and poorer fatigue limit. In this work, post-process micron-sized lasering is used to re-engineer additively manufactured stainless steel microstructures close to the sample surface in order to improve their overall performance. The key idea is to use smaller spot sizes and faster scan speeds during post-process lasering compared to the fabrication process. Using a novel coupling between a continuous-wave laser and a scanning electron microscope, single line scans were performed to optimise the lasering parameters. The optimised parameters were then used to treat the surface of the entire sample. The result is an intragranular structure refinement near the surface, exhibiting nearly an order of magnitude reduction in microsegregation cell and dislocation structure size, and increase in dislocation density. The ensuing microstructure demonstrates a higher yield strength without ductility loss and significant enhancement of the fatigue limit due to reduced surface roughness and intragranular structure refinement. The proposed technique has tremendous potential to improve the mechanical response of other alloys fabricated via additive manufacturing or any manufacturing technique.

Keywords

Laser treatment, mechanical behaviour, electron microscopy, fatigue, 3D printing

1. Introduction

One of the most important goals of research on engineering of stainless steels is to design microstructures that exhibit higher strength, ductility and fatigue limit than currently possible while reducing energy and material consumption. The advent of metal additive manufacturing (AM), has opened up the possibility to design as built (AB) parts with microstructures that present unprecedentedly higher strengths in comparison to their conventionally manufactured counterparts [1]. However, this increase in strength is often accompanied by a decrease in ductility and a poorer fatigue response [2], which is affected by a combination of material strength, surface roughness, defects (porosities or voids) and the residual stress state.

At the origin of the strength-ductility trade-off lies the hierarchical microstructure arising from the highly non-equilibrium processes occurring during AM. Heat-matter interaction induced melt pool dynamics, rapid solidification and solid-state thermal cycling result in a microstructure exhibiting physical and chemical heterogeneities ranging from few tens of nanometres to several hundreds of micrometres [3,4]. The primary contribution to material strength arises from the smallest of these features, which in stainless steels are precipitates, microsegregation cells and dislocation structures [5]. These intragranular features determine the mean free path of plastic deformation accommodating defects such as mobile dislocations. Typically, the smaller the size and higher the density of these features, the higher the strength and lower the ductility [1]. A commonly used approach to improve ductility is annealing, which is an isothermal heat treatment that evolves the metastable AB microstructure towards equilibrium by minimizing the stored energy. However, this process inadvertently causes an increase in feature size and decrease in density, inevitably resulting in a decrease in strength.

Meanwhile, the fatigue response of dense (negligible amount of porosities/voids) AB parts rely on the material strength as well as surface roughness [6]. During AM, unmelted powder particles sinter to the surface and become the dominant contributors to surface roughness of AB parts. Under fatigue loading, failure mainly occurs from surface crack nucleation (if not already present) and propagation in dense alloys. The fatigue response of AB parts can be improved via post-process surface treatments, the most common of which are mechanical in nature e.g., shot peening, polishing, etc., that induce in-plane compressive stresses on the surface and reduce surface roughness.

In this work, a non-isothermal heat treatment for AB parts is proposed in the form of continuous-wave (CW) laser scanning that simultaneously alters the underlying microstructure, specifically significantly refines the intragranular structure, and improves surface quality. The key idea is to perform this laser scanning using spot sizes and scanning speeds that are respectively smaller and faster than those used to build the samples in order to simultaneously improve the surface roughness and alter the intragranular microstructure.

This idea has been motivated by the microstructural differences between AB stainless steels fabricated via two commonly used techniques: CW laser-based powder bed fusion (LPBF) and CW laser-based direct energy deposition (LDED). However, LPBF processes use smaller laser spot sizes and faster scanning speeds than LDED processes. Consequently, stainless steel microstructures fabricated via LPBF exhibit smaller and denser features, and hence higher strength and lower ductility, than the LDED ones [4]. In this work, LDED stainless steel samples were used as base material and their surfaces were laser scanned using spot sizes and scan speeds

corresponding to LPBF. Note that while post-process laser-based surface treatments have been to polish surfaces of AM alloys [7,8] i.e., to reduce their surface roughness, it has not been used to simultaneously refine the intragranular structure and improve surface roughness, both of which are important to improve the overall mechanical response of a material.

Identifying appropriate laser scanning parameters to obtain a desired microstructure requires performing a parametric study in conjunction with microstructure characterisation before and after lasering. To facilitate such studies, a recently designed novel coupling between a CW laser and an environmental scanning electron microscope (CW laser-SEM (Fig. 1a,b)) [9] is used. While there are precedents for coupling between pulsed lasers and SEM [10–13], none exist for a CW laser-SEM. An important advantage of this coupling is its ability to perform laser scanning under secondary vacuum (pressure < 10^{-4} mbar) or under a controlled environment (e.g., inert gas environment) inside the environmental SEM. It prevents surface oxidation during lasering and facilitates a one-to-one comparison before and after scanning without additional surface preparation using different detectors available inside the SEM. The CW laser-SEM device is used to first perform a parametric study to optimise the lasering parameters.

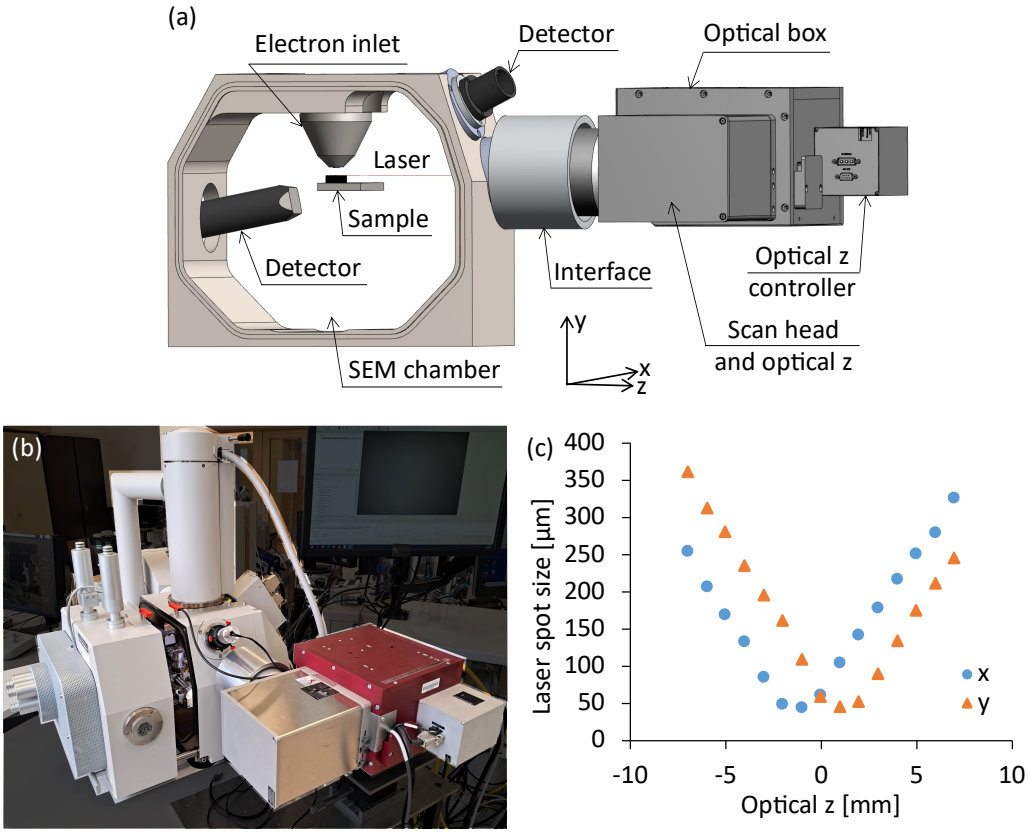

Fig. 1: CW laser-SEM coupling; illustration of the CW laser-SEM coupling (a) and image of the experimental setup (b). (c) Plot quantifying the laser spot sizes (1.7 times the full width at half maximum) in the *x* and *y* directions (in (a)) as a function of optical z (focusing distance controller).

The article is divided as follows: the experimental procedure and methods, including the CW laser-SEM, are described in section 2. Section 3 presents results and discussion around the parametric study, and tensile and fatigue testing. Finally, the conclusions of the study are presented.

2. Material and methods

2.1 Material

The materials studied in this work are two 316L stainless steels with different Si content. Henceforth, they are called 316L and 316L-Si. Wrought alloys are used to manufacture 316L and 316L-Si powders via inert gas atomisation by Oerlikon GMBH (Germany). The 316L powder has the following composition in weight percent (wt. %): Fe – balance, Cr – 17.34, Ni – 12.55, Mo – 2.34, Mn – 1.4, Si – 0.49, N – 0.08, Cu – 0.04, O – 0.03, P – 0.01, C < 0.1 and S < 0.1. Meanwhile, 316L-Si has the following composition in wt. %: Fe – balance, Cr – 17, Ni – 12, Mo – 2.5, Mn – 1.0, Si – 2.3, P < 0.1, C – 0.03 and S < 0.1. Granulometry reveals powder particle size range in between 45 μm and 90 μm.

2.2 Additive manufacturing via LDED

Thin walls with dimensions of 100 (x) × 12 (y) × 0.8 (z) mm^3 (for tensile testing) and 160 (x) × 30 (y) × 0.8 (z) mm^3 (for fatigue testing) were printed using a BeAM Modulo 400 LDED machine equipped with a 500W YLR-fibre laser. The printing process employed a bidirectional scanning strategy with a laser power of 250 W, scanning speed of 2000 mm/min, a powder flow rate of 6.8 g/min, a vertical displacement of focusing head of 0.2 mm after each layer deposition and a spot size of 0.7 mm.

2.3 CW laser-SEM coupling and sample polishing

The key equipment used in this work is the CW laser-SEM [9]. It is comprised of a coupling between a 1070 nm wavelength SPI QUBE 200 W air-cooled fibre laser (Industrial Laser Systems, France) and a FEI Quanta 600 environmental-SEM for characterisation (see Fig. 1a,b). The laser power can be varied from 9 to 209 W, the scanning speed from 0.01 to 20000 mm/s and the spot size from 45 to 500 μm with the help of the incorporated Scanlab varioscan$_{de}$20i type 133 (optical z). Virtually full 2D scanning liberty in a relatively large area (100 × 100 mm^2) is possible with the equipped Scanlab intelliscan III 20 scanner. The laser spot sizes as a function of optical z (see Fig. 1c) and the power have been calibrated using the femto easy BP 13.9 beam profiler and gentec UP55N-40S-H9-D0 calorimeter.

Some AB 316L and 316L-Si thin-walls (excluding those used for fatigue testing) were polished using 320, 600, 1200, 2400 and 4000 grit SiC paper followed by 3 μm and 1 μm diamond paste polishing. The final polishing step involved active oxide polishing (OPA) suspension polishing for two and a half minutes. Next, the samples (except the ones used for fatigue) were subjected to electrochemical etching using 10%vol. oxalic acid aqueous solution to reveal the microsegregations during backscatter electron (BSE) imaging. Electron backscatter diffraction

(EBSD) was performed with 1 μm step size using a Symmetry® detector (Oxford Instruments). BSE imaging is performed using an angular back scatter detector from Thermofisher.

In addition to SEM, OM is performed using the Keyence VHX-100 microscope with a VH-Z100R objective.

2.4 Uniaxial tensile testing

Rectangular plates with dimensions of 35 × 12 × 0.8 mm^3 were machined from the 316L and 316L-Si walls using HERMLE U 630 T, perpendicular to the DED build direction. After that, they were polished using the procedure described in section 2.3. Some of the polished plates were clamped in a small region (~7 × 3 mm^2) on one side and subjected to laser scanning. Dogbone specimens were extracted from AB and lasered 316L and 316L-Si samples using Hermle U 630 T; sample sides were mirror polished before machining (and before lasering for lasered samples) to avoid surface roughness influence on the mechanical testing. The gauge region had the dimensions 8 × 4 × 0.5 mm^3 ensuring a minimum length to width ratio of 2 that corresponds to the JIS Z 2241 standard; respecting this condition is sufficient for a comparative study between AB and lasered samples. Two specimens per condition were tested on a microtest stage at a (quasi-static) loading rate of 2 μm/s. The use of a Sill Optics correctal camera and digital image correlation helped to obtain the mechanical behaviour of the samples. All samples failed in the gauge region. After failure, fractography was performed on the specimens using SE imaging.

2.5 Scanning transmission electron microscopy and lamellae preparation

Thin-film lamellae were extracted inside a FEI Helios Nanolab 660 dualbeam SEM microscope equipped with a focused ion beam. The lamellae have a thickness of ~100 nm. They were studied in the Titan^3 G2 TEM microscope, which is equipped with a Cs-probe corrector, STEM detectors and a SuperX detector. It also has the capability to perform energy dispersive X-ray spectroscopy in order to characterise the chemical composition of the lamellae. Spectroscopy was performed with an acquisition time of 1 hour under operating conditions of 20000 counts per second and 300 keV. The spectra were deconvoluted and quantified as described in [14].

2.6 Residual stress measurement – X-ray diffraction

The $\sin^2\Psi$ X-ray diffraction method was used to determine the stresses in the austenitic phase. This method is based on the measurement of Bragg peak positions for a given *hkl* reflection and for various directions of the scattering vector with respect to sample. Due to a significant absorption of X-rays by metallic alloys, the method allows measurements on surfaces. In the case of austenitic steels, the average depth penetrated by X-rays at $\Psi = 0$ is ~7.2 μm; the average measurement depth is defined as the depth at which 67% of the incoming intensity is reflected. Hence, the surface residual stress measures are average measures over this depth.

The residual stresses were evaluated on the surface of both sides of the specimen using the Ψ tilt method and an *in situ* diffractometer X-RAYBOT (manufactured by MRX, France). To statistically optimise the number of grains in diffraction conditions, an oscillation of +/- 5° on Φ and Ψ angles was applied during the peak's acquisitions. A collimator with a circular irradiated area with a diameter of 2.5 mm was used. The diffraction conditions were chosen in accordance with the NF EN 15305-2009 standard: Mn-K_α radiation at 0.2290 nm wavelength, voltage 20 kV,

current 1 mA, 311 (*hkl*) lattice plane, diffraction angle 2θ = 152°, 21 Ψ angles in the range [−37.27°, 39.23°] and ±5° oscillations in Φ/Ψ.

2.7 Fatigue testing

Rectangular plates with dimensions of 70 × 14 × 0.8 mm^3 were machined from the 316L printed walls using Hermle U 630 T, perpendicular to the DED build direction. After that, the plates were clamped into a customised fixture and laser scanned under secondary vacuum with scanning speed of 100 mm/s, power of 70 W, spot size of 60 µm and scan overlap of 50%, within the CW Laser-SEM chamber. As a result, a 60 × 12 mm^2 area in the centre of the plates was laser treated. Subsequently, fatigue samples with 8 × 4 × 0.8 mm^3 gauge volume and 32 mm blending fillet (adhering to the ASTM E466-21 standard) were machined from the processed area using Hermle U 630 T. Simultaneously, the AB fatigue samples were directly machined from the unprocessed rectangular plates.

Constant amplitude uniaxial tensile fatigue test was conducted on both AB and L70 samples, using a 10 kN load cell on a Material Testing System (MTS 810), employing a sinusoidal stress waveform with a stress ratio (R) 0.1 and a constant frequency of 40 Hz, at room temperature. The loading direction was set perpendicular to the DED build direction. In order to determine the fatigue strength (σ_f), the staircase method was employed. Here, the starting stresses (σ_{max}) are chosen below yield strength of AB and L70 316L samples, at 275 and 325 MPa. Note that, since the difference between number of cycles corresponding to 300 MPa and 275 MPa is large, a median stress of 287.5 MPa is used for the fatigue testing. The testing was interrupted at 3 × 10^6 cycles (run-outs) for samples that do not fail until that point. Fracture in all the failed samples occurred in the gauge region.

2.8 Surface roughness measurement

Surface roughness measurements for unpolished AB 316L and unpolished + lasered 316L samples were conducted following the ISO 25178 norm using Bruker Alicona optical system with a ring light illuminator to improve image quality. Surface texture images were captured using 20x objective lens with vertical resolution less than 13 nm, Lambda C (L_c) filter of 80 µm, and stitched together. MeasureSuite of Alicona was used to obtain S_a.

3 Results and discussion

The reference AB samples used are 316L and 316L-Si stainless steel thin walls manufactured via LDED on hot-rolled 316L substrates using a single-pass-per-layer bidirectional scanning strategy with P 250 W, v 33.33 mm/s and s 0.7 mm. These parameters result in a surface energy density $E_s = P/(v \cdot s) = 10.71$ J/mm^2. Electron backscatter diffraction (EBSD) imaging after mirror polishing and etching the AB sample reveals a weak texture and a bimodal grain size distribution due to long columnar grains along layer height with a tilt along the printing direction, and smaller equiaxed grains in between layers (Fig. 2).

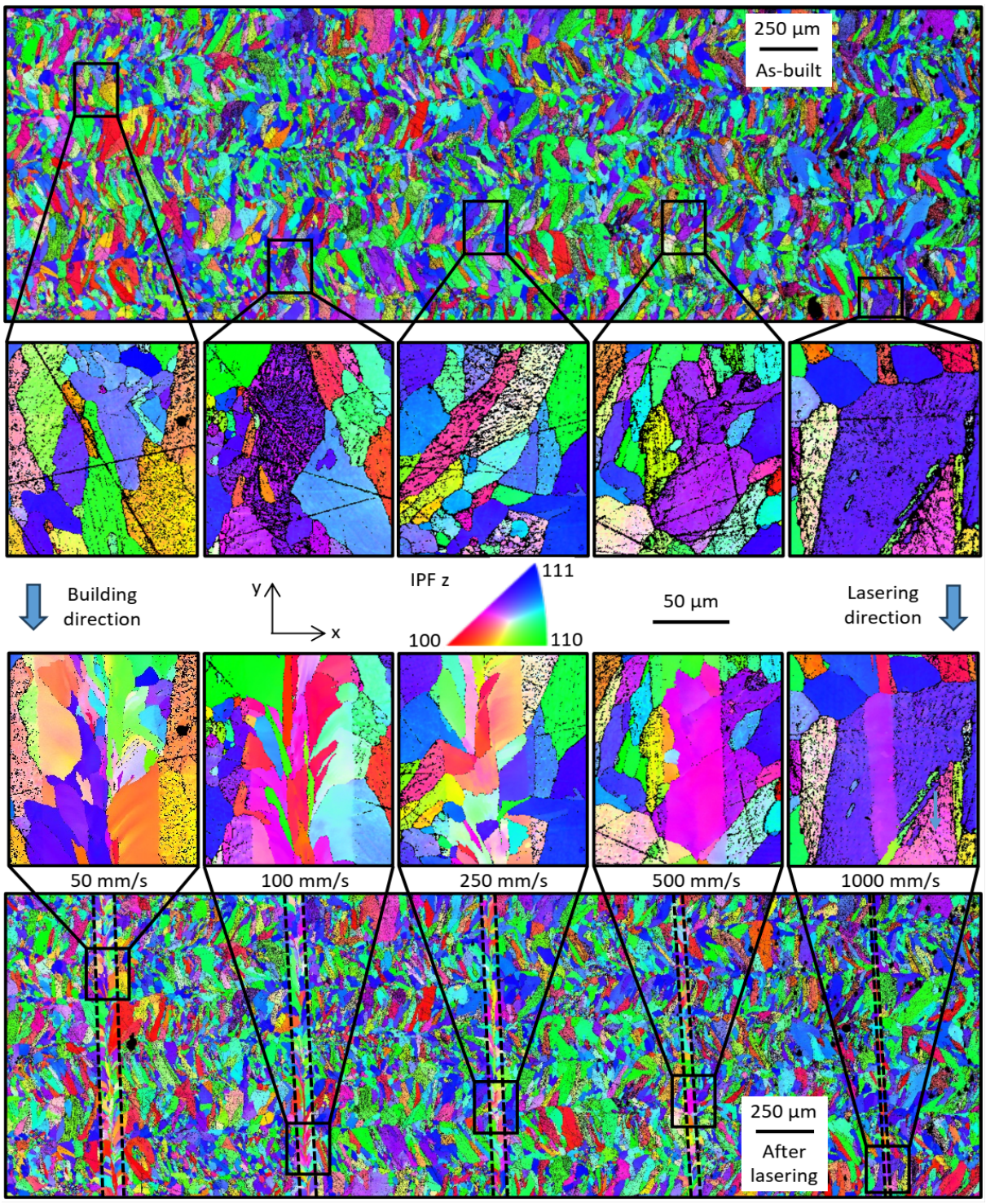

Fig. 2: EBSD IPF z images of the plane formed by building $(-y)$ and printing (x) directions of the polished AB LDED 316L thin-wall before and after laser scanning using s 60 µm, P 24 W and varying v (first parametric study). The noise (black dots) in the AB region of the EBSD maps is a consequence of surface undulations caused by chemical etching to facilitate BSE imaging of Cr-Mo microsegregations in Fig. 3.

3.1 Parametric post-process laser scanning studies

Two parametric laser scanning studies were first conducted with 316L inside the CW Laser-SEM under secondary vacuum. For both studies, a constant spot size s 60 µm was used; it is an order of magnitude smaller than the one used during LDED.

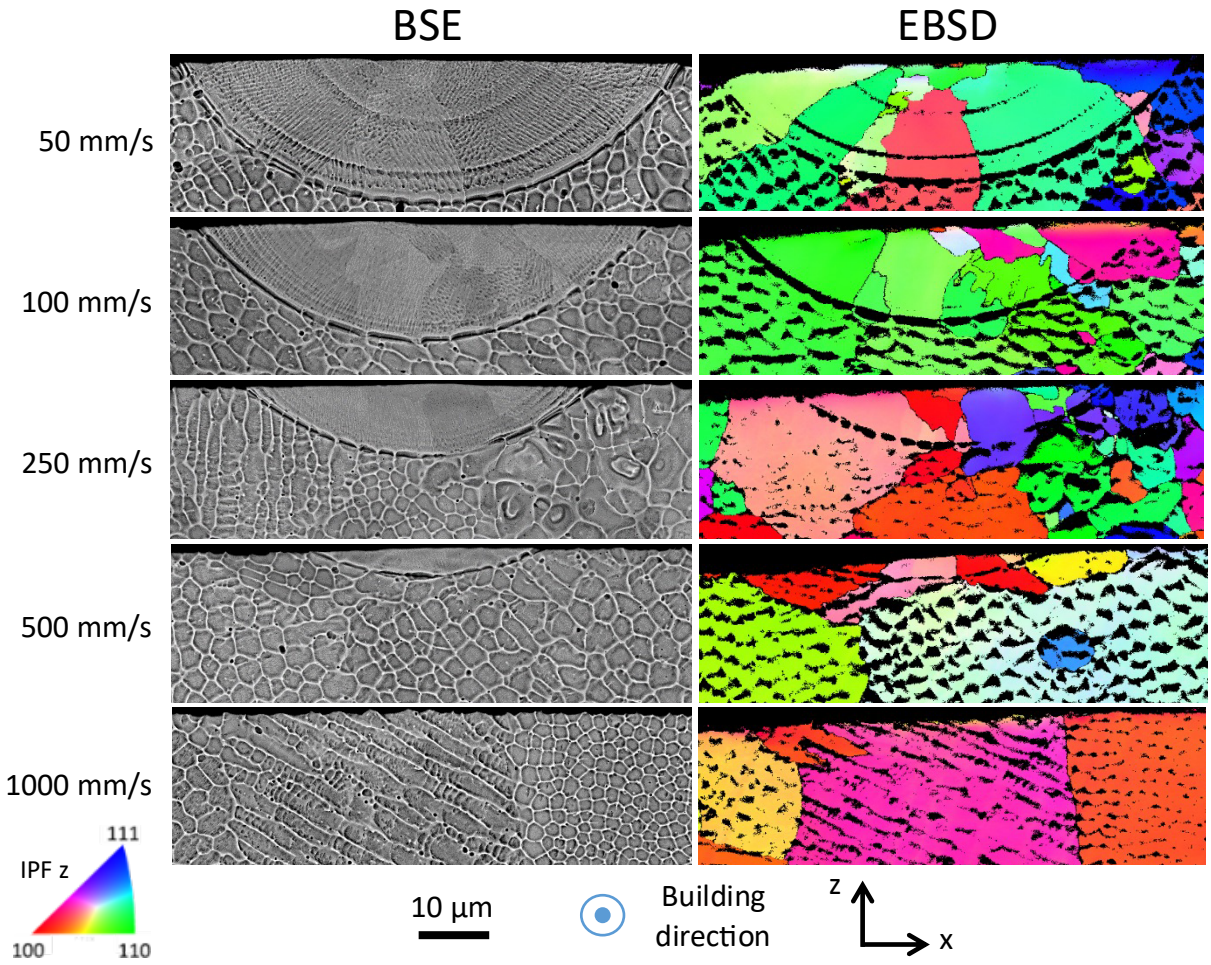

Fig. 3: BSE and EBSD IPF z images of the cross-sections across laser tracks studied in Fig. 2. The noise (black dots) in the AB region of the EBSD maps is a consequence of surface undulations caused by chemical etching to facilitate BSE imaging of Cr-Mo microsegregations. BSE and EBSD images share the same scale.

3.1.1 Varying scan speed, constant laser power and laser spot size

The first parametric study was performed to understand the role of varying E_s by varying v on microstructure alteration while keeping P, s and scan strategy constant. P was set at 10% of the maximum laser power, 24 W, which is the smallest stable value for the laser used. s was set to 60 µm, which is in the range of spot sizes used during LPBF. The scan strategy was a single line

scan along the y direction (Figs. 2,3). The laser scans were parallel to each other and separated by a distance of 0.8 mm from their neighbours as seen in Fig. 2 to avoid any influence of one scan on the other. The v were chosen to correspond to five different E_s lower than the one used to manufacture the samples; since the CW laser-SEM operates under vacuum and does not use any powder feedstock, there are no convection-related heat losses or powder-related laser reflection losses; hence, a lower E_s should be needed than during the LMD process to melt the material. The five different E_s (v) were: 8 J/mm^2 (50 mm/s), 4 J/mm^2 (100 mm/s), 1.6 J/mm^2 (250 mm/s), 0.8 J/mm^2 (500 mm/s) and 0.4 J/mm^2 (1000 mm/s). Laser scanning at the four highest E_s (four lowest v) results in melting, solidification and rapid cooling of the material, whereas laser scanning at the lowest E_s (highest v) results in heating and cooling without any melting (Figs. 2,3).

The melt pool sizes of the four remelted and solidified tracks (Fig. 3) expectedly decrease with decreasing E_s (increasing v) and their shapes reveal that conduction mode melting has occurred. The Cr and Mo microsegregation cells (a signature of rapid solidification in 316LSS [15,16]) in the lasered regions (Fig. 3) are at least an order of magnitude smaller than the ones in the AB material. Their size does not significantly decrease with increasing v, which was confirmed by comparing their sizes in the 50 mm/s and 500 mm/s tracks. The cell size difference between AB and lasered samples strongly indicates that solidification rates occurring during laser scanning are faster than those occurring during the LMD process, and they increase with increasing v. For the slowest laser scan (50 mm/s), the clearly visible microsegregation cells have an internal diameter that is ~300 nm on average. Assuming this value to be the primary cellular arm spacing (λ) during solidification, and using the empirical formula $\lambda = 80/\dot{T}^{1/3}$ for stainless steels [17], the deduced solidification rate ($\dot{T}$) in the slowest laser scanned region is $\sim 1.9 \times 10^7$ K/s; in comparison, the microsegregation cells in the AB 316L have a size of ~2.2 μm and the corresponding $\dot{T}$ is slower by three orders of magnitude. At such large solidification rates, and corresponding high temperature gradients, the γ-austenite grains epitaxially grow from the melt pool boundary via planar or cellular solidification mode and bend along the laser scanning direction [18], which is evidenced in the EBSD images in Figs. 2,3.

Following solidification, internal and sample constraints result in the formation of thermal stresses in the heat-affected solid. These stresses are sufficiently high to cause some of the grains to undergo plastic deformation e.g., via dislocation dynamics, which can be deduced from the presence of misorientation bands observed in some grains in the remelted zone (Fig. 2).

After lasering, a remarkably cleaner surface is obtained along all tracks. The cleaner surfaces are primarily a consequence of remelting and subsequent refinement of the microsegregation structure. A refined surface is also visible for the fastest laser scan, indicating that the surface could have slightly remelted even though it is not discernible in the BSE and EBSD images of the cross-section (Fig. 3).

3.1.2 Varying laser power, constant scan velocity and laser spot size

The next parametric study was performed to investigate laser penetration depth as a function of E_s but this time varying P and keeping v (50 mm/s), s (60 μm) and scan strategy (single line scan along the building direction) constant. Two different E_s were tested: 15 J/mm^2 (45 W – 20% of maximum P) and 22 J/mm^2 (66 W – 30% of maximum P) and compared with the laser

scan already performed at 8 J/mm^2 (24 W – 10% of maximum P). Based on the melt pool shapes (Fig. 4), the 8 J/mm^2 track resulted in conduction mode melting, whereas the 15 J/mm^2 and 22 J/mm^2 tracks resulted in keyhole mode melting. A pore can be observed close to the bottom of the melt pool in the 22 J/mm^2 laser track (black feature in the figure for 66 W), which is a signature of unstable keyhole mode melting. Such porosity is not visible in the 15 J/mm^2 track, however, the possibility of pores occurring elsewhere along the laser track cannot be eliminated.

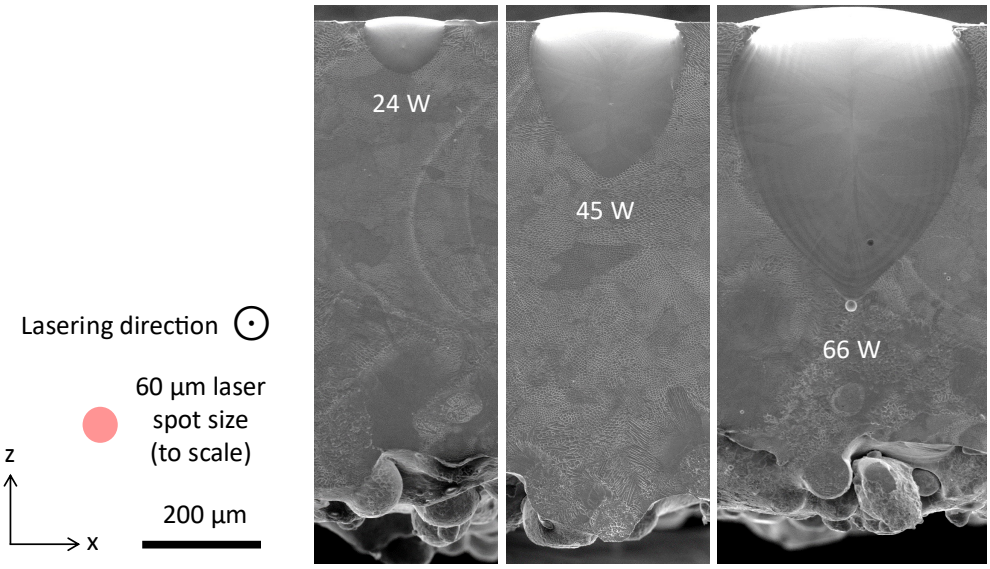

Fig. 4: BSE images showing the melt pool depths at the sample edge after lasering with s 60 µm, v 50 mm/s and varying P (second parametric study).

3.2 Summarising the parametric studies

In general, the melt pool depth increases with increasing E_s. It is more sensitive to P than to v; e.g., the depth triples when P is increased by a factor of 1.875 from 24 W, whereas it is halved when v is increased five-fold from 50 mm/s. A transition from conduction to keyhole mode melting occurs between 8 J/mm^2 and 15 J/mm^2. For all the scanning parameters used, cellular or planar grain growth occurs from the melt pool boundary during solidification; this deduction is supported by the crystallographic orientations and shapes of grains (Figs. 2, 3) and phase-field simulations aimed at understanding solidification during LPBF of 316L [18]. The newly formed grains have sizes similar to the unmelted ones in the base material and, as expected [18], they are bent along the direction of laser scanning. Following solidification, tensile residual stresses are generated along the laser track during cooldown as a consequence of the temperature gradient mechanism [19]. The local stresses can be sufficiently large to trigger dislocation dynamics causing local plastic deformation, as reported in a recent *in situ* synchrotron X-ray diffraction study [20]; this argument is further supported by the misorientation bands observed in the 50 mm/s track (Fig. 2). All laser scans result in a smoother surface, which can be deduced from the disappearance of noise in the EBSD maps caused by the reduction in surface undulations induced during etching.

Based on these studies, two key hypotheses can be derived. The smallest dislocation structures observed in both LDED and LPBF 316L typically either coincide with Cr-Mo

microsegregation cells [3] or they are smaller than these cells [21–23]. Furthermore, smaller the size of the microsegregation cells, smaller the dislocation structures and higher the dislocation density [3,21–23]. It is well accepted that smaller (tens of nanometres) and denser feature sizes strengthen the material. The first hypothesis (hypothesis 1) is that the material in the lasered zone should exhibit smaller and denser dislocation structures, and consequently higher strength, than the AB material. Meanwhile, the observed surface refinement after lasering suggests that laser scanning unpolished samples should reduce the surface roughness if the lasering causes local melting. The second hypothesis (hypothesis 2) is that, together with an increase in strength, these samples should exhibit an improved fatigue limit.

3.3 Tensile testing polished and lasered 316L and 316L-Si – improving strength-ductility tradeoff

Hypothesis 1 was tested by performing the following experiment. Six 35 mm-long pieces were machined from multiple AB 316L walls and polished on their largest surfaces (x and y in Fig. 2); the polishing was done to perform EBSD mapping before laser scanning and compare with the EBSD maps after laser scanning. In addition, four pieces of the same size were machined from LDED 316L-Si walls. Two polished 316L and 316L-Si walls were lasered on both sides (one side in its entirety before the other) using a bidirectional scan strategy with a 50% overlap (30 μm step) between two consecutive scans and an E_s of 11.67 J/mm^2 using P 35 W, s 60 μm, v 50 mm/s; these set of parameters, henceforth denominated L35, result in conduction mode melting, which is preferred from a manufacturing and service standpoint as it avoids creating keyhole porosities. Another two polished 316L walls were lasered on both sides with the same strategy and same E_s (11.67 J/mm^2), but double P and v i.e., with P 70 W, s 60 μm, v 100 mm/s (henceforth denominated L70). All laser scans were conducted under secondary vacuum. Dogbone shaped samples were extracted from all walls. Optical microscopy (OM), SEM, and scanning transmission electron microscopy (STEM) were performed before and after laser scanning. For an L70 316L sample, residual stresses were measured before and after lasering as well as after extracting the dogbone.

Polishing AB walls induces compressive stresses on their surfaces along both in-plane directions; e.g., a polished AB 316L wall exhibits $\sigma_{xx} \approx \sigma_{yy} \approx -75 \pm 20$ MPa. However, subsequent lasering on one face followed by the other results in bending and unbending of the walls and a significant alteration of the stresses; the same sample exhibits $\sigma_{xx} = 0 \pm 11$ MPa and $\sigma_{yy} = 271 \pm 39$ MPa on the first lasered surface and $\sigma_{xx} = 189 \pm 18$ MPa and $\sigma_{yy} = 350 \pm 41$ MPa on the second lasered surface. This difference in residual stress states before and after lasering implies that the sample has undergone plastic deformation during lasering. The residual stress state is further altered during dogbone extraction; the aforementioned sample exhibits $\sigma_{xx} = -57 \pm 21$ MPa and $\sigma_{yy} = 94 \pm 18$ MPa on the first surface and $\sigma_{xx} = 142 \pm 15$ MPa and $\sigma_{yy} = -34 \pm 20$ MPa on the second surface demonstrating a remarkable $\sim 135^\circ$ rotation of the in-plane stress vector.

Continuing to focus on 316L, the melt pool shapes in the lasered zones reveal that conduction mode melting had indeed occurred (Fig. 5a). The L35 and L70 scans have respectively penetrated 8% and 14% of the total thickness of the AB walls. Both scans result in the formation

of zig zag grains in accordance to the bidirectional scanning strategy used. L35 results in a weak texture, similar to the AB samples, but smaller grain sizes than the columnar grains of the AB samples (Fig. 5b). In contrast, L70 results in a strong <100> texture with grains traversing multiple tracks normal to the direction of lasering. Dislocation structures and density in the lasered region are respectively smaller and higher than in the AB samples, and dislocation structures mainly coincide with the microsegregations cells (Fig. 5c, d). While similar co-occurrence has been reported for LPBF 316L [3], microsegregation cells after L70 are richer in Ni-Cr-Mo-Mn-Si-O as opposed to only Cr-Mo ones reported in [3]. Furthermore, microsegregation cells in L70 samples are decorated with Mn-Si-rich oxide precipitates that are smaller in size and more evenly distributed than those occurring in LDED 316L.

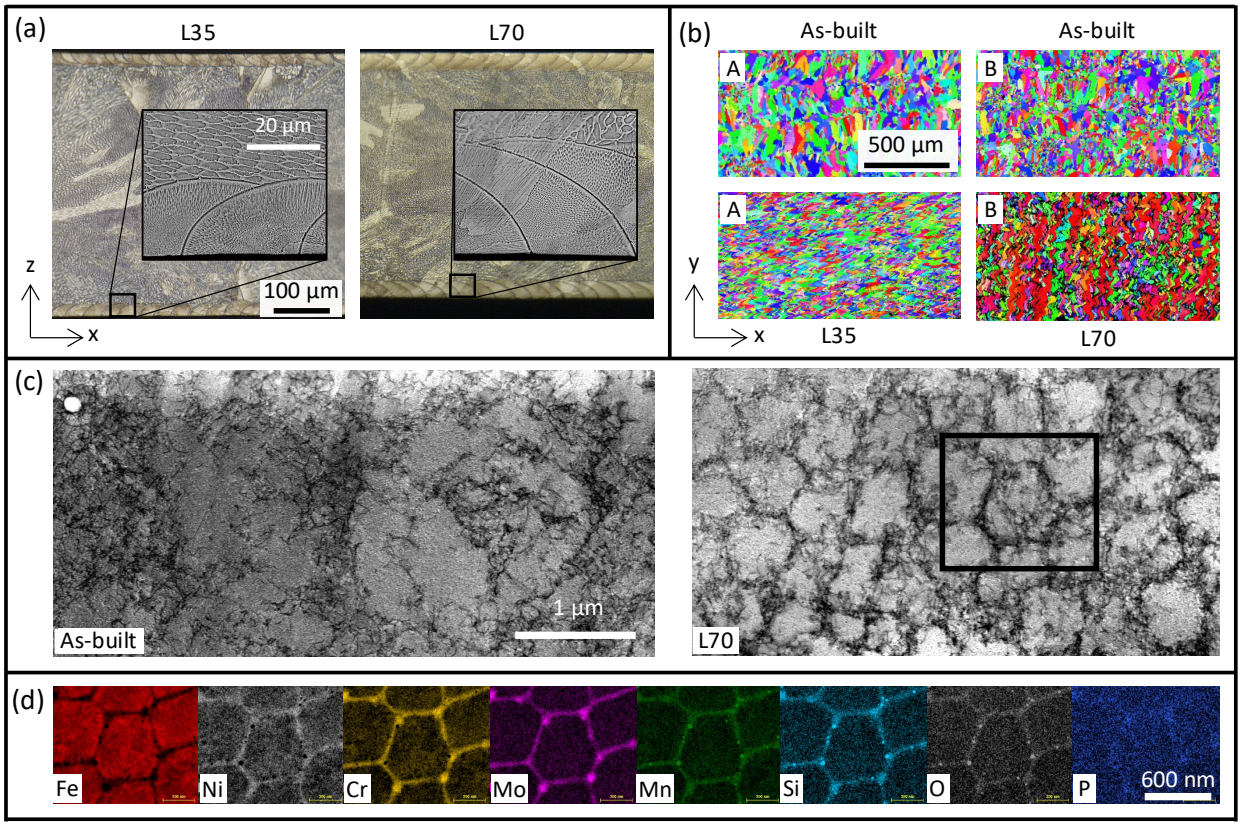

Fig. 5: (a) OM (inset BSE) images of the cross-sections of L35 and L70 316L samples. (b) EBSD images of the surface of 316L before and after L35 (A) and L70 (B). (c) Bright-field STEM images of lamellae extracted from AB and L70 316L. (d) Energy dispersive X-ray spectroscopy images from L70 revealing chemical content in the region indicated with a black box in (c).

Tensile testing reveals that AB 316L and 316L-Si exhibit a mean yield strength of 360 MPa and 414 MPa, respectively (Fig. 6a). Focusing on 316L, L35 and L70 result in an improvement of the mean yield strength by 11.67% and 31.11%. Using the rule of mixtures, the mean yield strengths of the lasered zones in L35 and L70 are found to be 884 MPa and 1157 MPa, respectively. To the best of our knowledge, such high yield strengths have never been reported for 316L fabricated either via LDED or LPBF.

Meanwhile, L35 316L-Si exhibits a mean yield strength of 469 MPa (an increase by 13.29%). These results together with the smaller denser dislocation structures (Fig. 5c) in the lasered zones validate hypothesis 1.

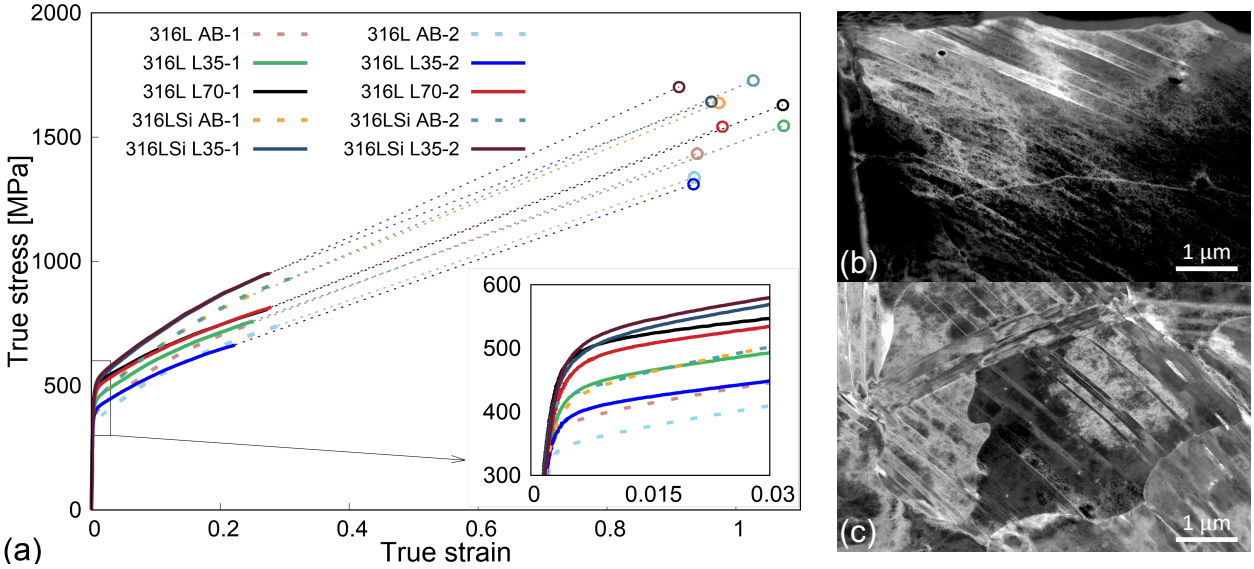

Fig. 6: (a) True stress-strain curves for AB, L35 and L70 316L and AB and L70 316L-Si. The circles represent the stresses and strains at failure of each sample. The small dotted lines are linear connectors between the end of strain measurement and the sample failure. The inset shows a zoomed in view of the boxed region. Post-deformation dark-field STEM images of lamellae taken from (b) AB and (c) lasered zone of L70 316L samples. The 316L AB-1 and L35-1 samples have been extracted from one wall and AB-2 and L35-2 from another wall; thus, while there is a difference in strength between the two AB samples of these walls, yet L35 results in a significant increase in strength for both.

All samples fulfil the Considère criterion (Fig. 7), which means all microstructures achieve their full deformation capability prior to failure. This result is further corroborated by fractography studies (Fig. 8) showing the perfect bonding between lasered and AB regions; interestingly, the lasered region in L70 shows smaller voids, caused due to ductile damage, than in the AB region underneath as well as in the AB sample. This implies that post-process laser scanning has not adversely affected the ductility of 316L and 316L-Si. In fact, L70 has resulted in a slight (9.4%) improvement in ductility of 316L (Fig. 6a). Therefore, laser scanning has resulted in a net increase in the strength-ductility tradeoff for both materials.

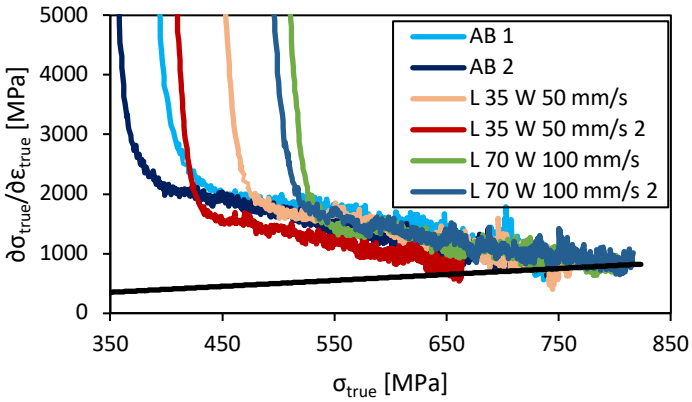

Figure 7: Tangent modulus of the true stress-strain curve as a function of the true stress for all the 316L tensile testing samples. The black line indicates the Considère criterion.

In order to better understand the origin of no change (and even a slight improvement) in ductility, TEM lamellae extracted post-mortem from AB and L70 316L samples were analysed via scanning TEM. The analysis revealed that while permanent deformation in the AB 316L sample was accommodated via dislocation structure evolution, significant deformation twinning along with dislocation structure evolution had occurred in the L70 316L sample (Fig. 6b, c for AB and L70 316L, respectively); these results were confirmed with selective area diffraction maps (not shown here) and the observation of newer and smaller (than the microsegregation) dislocation cells in both AB and L70 316L samples. EDS analysis revealed that the microsegregations were not affected indicating that in the L70 sample, the finer cells do not prevent twin propagation and dislocation structure evolution. The fact that both deformation twinning and dislocation structure evolution occur in the L70 sample explain why ductility is not adversely affected after lasering.

It should be noted that not all materials will have the possibility to accommodate deformation via multiple micromechanisms such as those occurring in 316L and therefore such an improvement in the strength-ductility tradeoff should not be *a priori* assumed for other materials.

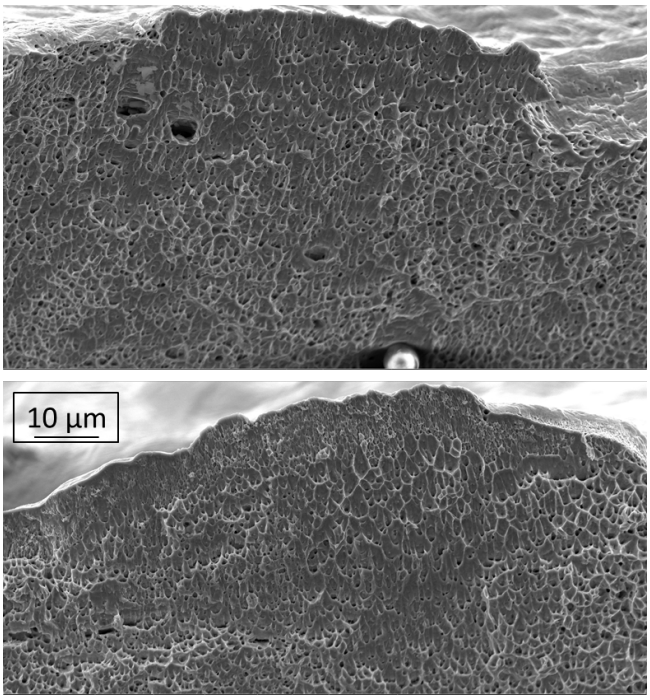

Figure 8: Fractography of AB (Top) and L70 (bottom) 316L samples. The scale for both samples is shown in the bottom image.

3.4 Fatigue testing unpolished and lasered samples – fatigue limit enhancement

Hypothesis 2 is validated with the following experiment. Multiple 70-mm long unpolished AB 316L walls were laser scanned under secondary vacuum on both surfaces via L70. The surface roughness improved considerably with the mean surface height (S_a) decreasing from 16.593 µm on AB samples to 0.902 µm after L70. Dogbone samples were extracted from unpolished AB and lasered 316L walls and subjected to tension-tension fatigue at varying stress amplitudes and mean values. Despite the presence of tensile residual stresses due to lasering, L70 results in a significant (~25%) increase in the fatigue limit (Δσ) from 181.94 MPa for the AB sample to 227.24 MPa (Fig. 9). This improvement is a combined consequence of intragranular structure refinement (and the accompanying yield strength increase) along with the reduction in surface roughness.

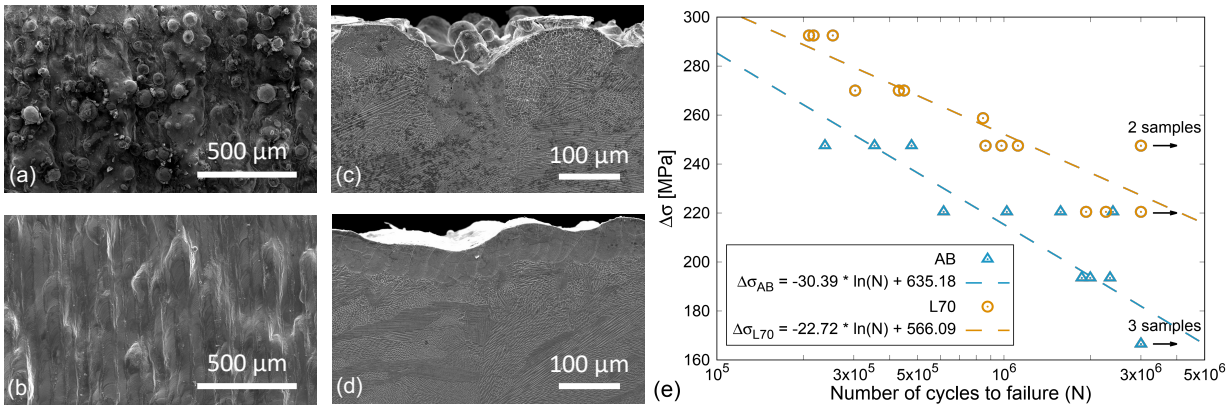

Fig. 9: Secondary electron (SE) images of the (a, b) surfaces and (c, d) cross-sections of (a, c) unpolished AB and (b, d) L70 316L walls. (e) Wöhler (S-N) curve with double the stress amplitude ($\Delta\sigma$) vs number of cycles to failure (N) for tension-tension fatigue cycling of unpolished AB and lasered 316L samples. The trendlines are plotted for both samples and the arrows indicate fatigue runout cut-off at 3 million cycles.

4 Conclusions and perspectives

In this work, 316L and 316L-Si stainless steel thin-walls fabricated via the LDED process were subjected to post-process laser scanning inside the secondary vacuum of a newly designed system coupling a continuous-wave laser and an environmental SEM, called CW laser-SEM. The two widest surfaces of the LDED thin-walls were laser scanned using parameters similar to those used in LPBF processes. The results clearly demonstrate that lasering surfaces of as built (AB) stainless steels, using smaller spot sizes and faster scan speeds than those used during fabrication, can simultaneously significantly improve their strength-ductility trade-off and the fatigue limit. Notably,

- Laser scanning resulted in the formation of sandwiched microstructures exhibiting an intragranular structure refinement in the laser melted region in comparison to the base as built (AB) material. In fact, an order of magnitude reduction in the intragranular segregation cells and dislocation cell structure was achieved in the laser scanned region, which resulted in an increase in the overall yield strength of the sample. In one case, an overall increase in the yield strength by 31.11% over the 360 MPa of the AB material was obtained after laser scanning. For this sample, the laser penetration depth (where melting had occurred) was only 14% of the total depth of the sample. Consequently, through the rule of mixtures, a yield strength of ~1.15 GPa was obtained in the lasered region, which is significantly higher than the typical yield strengths achieved via LPBF of 316L.
- This increase in yield strength occurs without any ductility loss (and even a slight improvement in one case) indicating an overall improvement in the strength-ductility tradeoff. A deeper investigation in the case of lasered 316L reveals that this improvement occurs because plastic deformation is accommodated via dislocation structure evolution as well as deformation twinning in the lasered region.
- The strength enhancement, together with the surface roughness reduction due to laser scanning, translates into a significant improvement in fatigue life. An increase in fatigue limit by 25% was obtained for 316L.

Along with these results, a plethora of new interesting findings are presented, which merit deeper investigations in the future. These include (i) generation of residual stresses with strongly varying principal stresses across the sample thickness, (ii) grain structure and texture formation as a function of scan strategies keeping the energy density constant, (iii) coincidence of Ni-Mn-Si-O-rich segregations with the expected Cr-Mo segregations during solidification, (iv) reduction in the strain hardening effect after laser scanning, (v) the precise contributions of surface roughness reduction and intragranular structure refinement on fatigue limit improvement, etc.

The post-process CW lasering approach has promising prospects. For example, it can be integrated within an AM process, potentially minimising or eliminating the need for extensive

post-processing steps and enabling the production of net-shaped parts with superior mechanical properties. Furthermore, it creates new avenues for optimising performance of not only AM stainless steels but also other alloys, including those manufactured using other techniques.

Acknowledgments

The authors acknowledge the support of the following people: Pierre-Louis Hanappier (LMS) for printing the 316L samples, Nathalie Isac (LMS) for printing the 316L-Si samples, Simon Hallais (LMS) for discussions regarding SEM, Hind Meissera for assisting with the fatigue testing during their internship at LMS, and Eva Héripré (PIMM) for discussions on TEM lamellae preparation. JGSM, KC and MVU are grateful to the European Research Council (ERC) for their support through the European Union's Horizon 2020 – EXCELLENT SCIENCE – research and innovation program (grant agreement number 946959). All authors would like to thank LMS for providing financial support to build the CW Laser-SEM system.

Declaration of Competing Interest

The authors declare that they have no known competing financial interests or personal relationships that could have appeared to influence the work reported in this paper.

CRediT authorship contribution statement

Juan Guillermo Santos Macías: Conceptualisation, Data Curation, Formal analysis, Investigation, Methodology, Validation, Visualisation, Writing – original draft, Writing – review & editing.
Kewei Chen: Formal analysis, Investigation, Validation, Visualisation, Writing – review & editing.
Alexandre Tanguy: Conceptualisation, Formal analysis, Investigation, Validation, Methodology, Writing – review & editing.
Maxime Vallet: Investigation, Visualisation, Writing – review & editing.
Louis Cornet: Investigation, Visualisation, Writing – review & editing.
Vincent Michel: Investigation, Visualisation, Writing – review & editing.
Upadhyay Manas Vijay: Conceptualisation, Formal analysis, Funding acquisition, Investigation, Methodology, Project administration, Resources, Supervision, Writing – original draft, Writing – review & editing, Validation, Visualisation.

Data availability: Data sets generated during the current study are available from the corresponding author on reasonable request.

Code availability: No code has been developed for this work.

References

[1] T. DebRoy, H.L. Wei, J.S. Zuback, T. Mukherjee, J.W. Elmer, J.O. Milewski, A.M. Beese, A. Wilson-Heid, A. De, W. Zhang, Additive manufacturing of metallic components -

Process, structure and properties, Prog. Mater. Sci. 92 (2018) 112–224. https://doi.org/10.1016/j.pmatsci.2017.10.001.
[2] T.M. Mower, M.J. Long, Mechanical behavior of additive manufactured, powder-bed laser-fused materials, Mater. Sci. Eng. A 651 (2016) 198–213. https://doi.org/10.1016/j.msea.2015.10.068.
[3] Y.M. Wang, T. Voisin, J.T. McKeown, J. Ye, N.P. Calta, Z. Li, Z. Zeng, Y. Zhang, W. Chen, T.T. Roehling, R.T. Ott, M.K. Santala, P.J. Depond, M.J. Matthews, A.V. Hamza, T. Zhu, Additively manufactured hierarchical stainless steels with high strength and ductility, Nat. Mater. 17 (2018) 63–71. https://doi.org/10.1038/nmat5021.
[4] J. Bedmar, A. Riquelme, P. Rodrigo, B. Torres, J. Rams, Comparison of different additive manufacturing methods for 316L stainless steel, Mater. 14 (2021) 6504. https://doi.org/10.3390/ma14216504.
[5] Md. Shamsujjoha, S.R. Agnew, J.M. Fitz-Gerald, W.R. Moore, T.A. Newman, High strength and ductility of additively manufactured 316L stainless steel explained, Metall. Mater. Trans. A 49 (2018) 3011–3027. https://doi.org/10.1007/s11661-018-4607-2.
[6] Y. Murakami, Metal Fatigue: Effects of Small Defects and Nonmetallic Inclusions, 2nd ed., Academic Press, Elsevier, Cambridge, MA, USA, 2019.
[7] L. Chen, B. Richter, X. Zhang, X. Ren, F.E. Pfefferkorn, Modification of surface characteristics and electrochemical corrosion behavior of laser powder bed fused stainless-steel 316L after laser polishing, Addit. Manuf. 32 (2020) 101013. https://doi.org/10.1016/j.addma.2019.101013.
[8] C. Li, D. Liu, G. Liu, S. Liu, X. Jin, Y. Bai, Surface characteristics enhancement and morphology evolution of selective-laser-melting (SLM) fabricated stainless steel 316L by laser polishing, Opt. Laser Technol. 162 (2023) 109246. https://doi.org/10.1016/j.optlastec.2023.109246.
[9] A. Tanguy, M.V. Upadhyay, J.G. Santos Macías, Système pour traiter par laser à onde continue et caractériser par MEB un échantillon (Patent Pending - deposited on 16 December 2022), (Patent Pending), n.d.
[10] K. Wetzig, J. Edelmann, W. Fischer, H. Mueller, LASEM - a novel combined device for laser modification in SEM, Scanning 9 (1987) 99–107. https://doi.org/10.1002/sca.4950090303.
[11] A.H. Foitzik, M.W. Füting, G. Hillrichs, L.-J. Herbst, In situ laser heating in an environmental scanning electron microscope, Scanning 19 (1997) 119–124. https://doi.org/10.1002/sca.4950190211.
[12] M.P. Echlin, N.S. Husseini, J.A. Nees, T.M. Pollock, A new femtosecond laser-based tomography technique for multiphase materials, Adv. Mater. 23 (2011) 2339–2342. https://doi.org/10.1002/adma.201003600.
[13] P.F. Rottmann, A.T. Polonsky, T. Francis, M.G. Emigh, M. Krispin, G. Rieger, M.P. Echlin, C.G. Levi, T.M. Pollock, TriBeam tomography and microstructure evolution in additively manufactured Alnico magnets, Mater. Today 49 (2021) 23–34. https://doi.org/10.1016/j.mattod.2021.05.003.
[14] M.V. Upadhyay, M.B.H. Slama, S. Gaudez, N. Mohanan, L. Yedra, S. Hallais, E. Héripré, A. Tanguy, Non-oxide precipitates in additively manufactured austenitic stainless steel, Sci. Rep. 11 (2021) 10393. https://doi.org/10.1038/s41598-021-89873-2.
[15] S. Kou, Welding metallurgy, John Wiley & Sons, New Jersey, 2003.

[16] K.G. Prashanth, J. Eckert, Formation of metastable cellular microstructures in selective laser melted alloys, J. Alloy. Compd. 707 (2017) 27–34. https://doi.org/10.1016/j.jallcom.2016.12.209.
[17] Th. Schubert, W. Löser, S. Schinnerling, I. Bächer, Alternative phase formation in thin strip casting of stainless steels, Mater. Sci. Technol. 11 (1995) 181–185. https://doi.org/10.1179/mst.1995.11.2.181.
[18] A.F. Chadwick, P.W. Voorhees, The development of grain structure during additive manufacturing, Acta Mater. 211 (2021) 116862. https://doi.org/10.1016/j.actamat.2021.116862.
[19] P. Mercelis, J. Kruth, Residual stresses in selective laser sintering and selective laser melting, Rapid Prototyp. J. 12 (2006) 254–265. https://doi.org/10.1108/13552540610707013.
[20] S. Gaudez, K.A. Abdesselam, H. Gharbi, Z. Hegedüs, U. Lienert, W. Pantleon, M.V. Upadhyay, High-resolution reciprocal space mapping reveals dislocation structure evolution during 3D printing, Addit. Manuf. 71 (2023) 103602. https://doi.org/10.1016/j.addma.2023.103602.
[21] T.R. Smith, J.D. Sugar, C. San Marchi, J.M. Schoenung, Strengthening mechanisms in directed energy deposited austenitic stainless steel, Acta Mater. 164 (2019) 728–740. https://doi.org/10.1016/j.actamat.2018.11.021.
[22] A.J. Birnbaum, J.C. Steuben, E.J. Barrick, A.P. Iliopoulos, J.G. Michopoulos, Intrinsic strain aging, Σ3 boundaries, and origins of cellular substructure in additively manufactured 316L, Addit. Manuf. 29 (2019) 100784. https://doi.org/10.1016/j.addma.2019.100784.
[23] K.M. Bertsch, G. Meric De Bellefon, B. Kuehl, D.J. Thoma, Origin of dislocation structures in an additively manufactured austenitic stainless steel 316L, Acta Mater. 199 (2020) 19–33. https://doi.org/10.1016/j.actamat.2020.07.063.